Adaptive glasses wavefront sensorless Full-Field OCT for high-resolution retinal imaging over a wide field-of-view

Pedro Mecê, Jules Scholler, Kassandra Groux, Kate Grieve, Claude Boccara

Adaptive glasses wavefront sensorless Full-Field OCT for high-resolution retinal imaging over a wide field-of-view

Pedro Mecê[a,b], Jules Scholler[a], Kassandra Groux[a], Kate Grieve[c], and Claude Boccara[a]

[a]Institut Langevin, ESPCI Paris, CNRS, PSL University, France
[b]DOTA, ONERA, Université Paris Saclay F-91123 Palaiseau, France
[c]Paris Eye Imaging Group, Quinze Vingts National Ophthalmology Hospital, Paris, France

ABSTRACT

The highest three-dimensional (3D) resolution possible in *in-vivo* retinal imaging is achieved by combining optical coherence tomography (OCT) and adaptive optics. However, this combination brings important limitations, such as small field-of-view and complex, cumbersome systems, preventing so far the translation of this technology from the research lab to clinics. Here, we mitigate these limitations by combining our compact time-domain full-field OCT (FFOCT) with a multi-actuator adaptive lens positioned just in front of the eye, in a technique we call the adaptive-glasses wavefront sensorless approach. Through this approach, we demonstrate that ocular aberrations can be corrected, increasing the FFOCT signal-to-noise ratio and enabling imaging of different retinal layers with a $2\mu m \times 2\mu m \times 8\mu m$ resolution over a $5^o \times 5^o$ field-of-view, without major anisoplanatism influence.

Keywords: Optical Coherence Tomography, Adaptive Optics, Retinal Imaging, Photoreceptors, Nerve Fiber Layer

1. INTRODUCTION

Optical coherence tomography (OCT) revolutionized ophthalmology in the 1990s owing to its high axial resolution, which enabled clinicians to distinguish the retinal layers *in-vivo*.[1] Although the axial resolution of OCT is sufficient to resolve retinal features at a micrometer scale, the lateral resolution is limited by ocular aberrations.[2] Owing to its capacity to correct for ocular aberrations in real-time, adaptive optics (AO) has become the primary technique to achieve high lateral resolution in the retina.[3] When coupled to OCT, AO has enabled micrometer resolution in all spatial dimensions for *in-vivo* retinal imaging,[4] contributing to the understanding of retinal function[5] and diseases.[6] Nevertheless, the high lateral resolution achieved with AO comes with a cost of a small field-of-view (FOV), which is limited by the isoplanatic patch of the eye (around $2^o \times 2^o$)[7] but also by the trade-off between the spatial sampling of the scan and the acquisition speed, in order to avoid image distortion due to involuntary fixational eye motion.[8] Most importantly AO-OCT systems are complex and cumbersome, requiring long imaging sessions to acquire a large FOV.[4] These limitations have prevented the translation of AO-OCT from the research lab to clinics. Much recent work has aimed at addressing these limitations, by reducing the AO-OCT system complexity and footprint through the use of conjugated lens-based wavefront sensorless AO,[9,10] or by increasing the FOV to $4^o \times 4^o$ using multi-conjugate AO.[11] However, the former still presents a small FOV because of the limited isoplanatic patch of the eye and spatial sampling of the scan, and the latter adds complexity as two deformable mirrors are necessary.

In this manuscript, we propose a lens-based sensorless AO approach using a multi-actuator adaptive lens (MAL) positioned in front of the examined eye, *i.e.* without strict pupil conjugation, in a technique we call the adaptive-glasses approach. The proposed optimization scheme does not require any calibration step and is therefore straightforward to implement in existing systems without increasing system footprint or optical complexity. We implemented the adaptive-glasses approach in our compact time-domain full-field OCT (henceforth, named FFOCT) system. FFOCT was found to behave differently to conventional imaging systems and Fourier-domain

Further author information:
P.M.: E-mail: pedrofbmece@gmail.com

OCT with regards to optical aberrations. The lateral resolution of FFOCT is less affected by symmetric aberrations (*i.e.* defocus and astigmatism),[12] which dominate in the eye, owing to the use of a spatially incoherent source. This interesting feature was recently highlighted for high-resolution retinal imaging over a field-of-view of $3.5^o \times 3.5^o$, without apparent anisoplanatism.[13] Nevertheless, although symmetrical aberrations may not be adversely affecting the resolution in FFOCT, the presence of aberrations still provokes a loss of signal-to-noise ratio (SNR). Low SNR strongly impacts the robustness of FFOCT imaging, especially at large pupil size, and prevents imaging of retinal layers other than photoreceptors.[13,14] Here, we show that the use of the adaptive glasses approach to correct for ocular aberrations can considerably increase the SNR and robustness of FFOCT, enabling imaging of different retinal layers with 3D cellular resolution over a $5^o \times 5^o$ FOV acquired in a single shot, while retaining a compact system design. To the best of our knowledge the presented method is the first to ally 3D high-resolution, wide FOV, high acquisition rate and small system footprint, which are essential characteristics for clinical deployment.

2. METHODS

2.1 Description of the FFOCT system

Figure 1(a,b) presents the optical and mechanical schematic of the FFOCT system, outlining the low optical complexity and reduced footprint ($50cm \times 30cm$). Figure 1(c) shows the first FFOCT prototype, which was recently installed at the Quinze-Vingts National Ophthalmology Hospital (Paris, France). To date, five different users (two of which trained) have already used the systems alone to acquire retinal images from subjects.

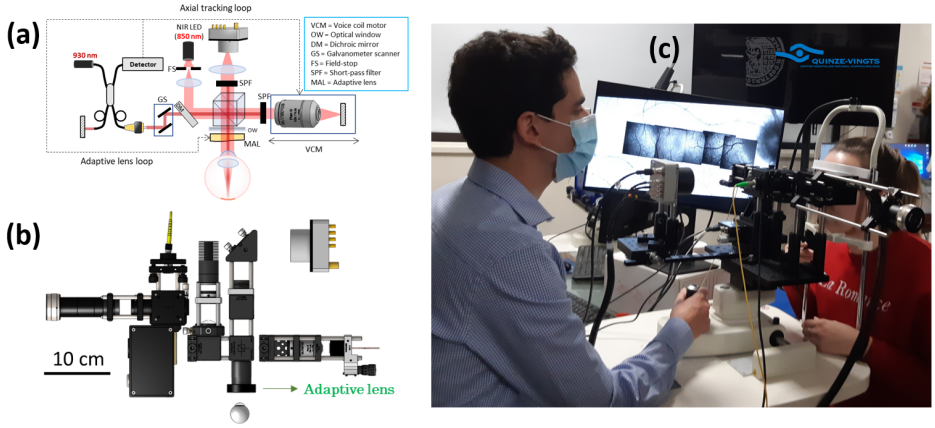

Figure 1. Optical **(a)** and mechanical **(b)** drawing outlining the low optical complexity and reduced footprint of the custom-built FFOCT for retinal imaging. **(c)** Prototype installed at the Quinze-Vingts National Ophthalmology Hospital.

The main components of the custom-built FFOCT system used in this study have been previously described in detail elsewhere.[14] In brief, the FFOCT comprises a light-emitting diode (LED) with central wavelength of 850nm (30nm bandwidth), used as a spatially incoherent illumination source, giving a theoretical axial resolution of approximately 8 μm in water. The illumination beam is split into reference and sample arms by a 50:50 cubic beam splitter (BS). For the reference arm, a microscope objective is used with a silicon mirror placed at the focal plane of the objective. For the sample arm, the subject's eye was aligned along the optical axis. The back-scattered photons from both arms are recombined by the same BS and focused onto a high-speed CMOS camera (Q-2A750-Hm/CXP-6, Adimec) for FFOCT imaging. The size of an individual pixel of the FFOCT camera corresponds to $1\mu m$ in the retinal plane. The FFOCT coherence gate geometry was shaped to fit the retinal curvature and dispersion was compensated using a 20mm N-BAK1 optical window in the sample arm.[13] The FFOCT system is coupled through a dichroic mirror with a spectral-domain (SD) OCT system, with central wavelength of 930nm (60nm bandwidth). The SD-OCT was used to track and correct for eye axial motion by driving at 50Hz loop rate a fast voice-coil translation stage on which the FFOCT reference arm is mounted (see[14] for further details). The correction in real-time of axial eye motion enables the FFOCT to acquire *en-face*

images at a given depth in the retina. The SD-OCT has an A-scan rate of 36kHz. We chose to scan over a line of 2^o FOV at 140 Hz, providing a good trade-off between acquisition speed and SNR.[14] For both FFOCT and SD-OCT channels, the beam diameter at the pupil is 7.5mm.

2.2 Adaptive-Glasses Wavefront Sensorless Approach

Since the phase modulation of FFOCT is performed almost randomly through the axial eye motion,[14] the brightness of FFOCT retinal images varies from one image to another, making the FFOCT signal an unreliable merit function for wavefront correction. We therefore use the brightness of the SD-OCT B-scan as a surrogate for the FFOCT SNR optimization. Once these two wavelengths are close, correcting aberrations using the brightness of SD-OCT as a merit function is also suitable for FFOCT. B-Scans were averaged in the lateral dimension, and used for three purposes: 1) tracking the eye axial motion for correction in real-time, 2) guiding positioning of the FFOCT coherence gate at the layer of interest, and 3) as a merit function for the wavefront optimization. The merit function can be applied for any retinal layer of interest to automatically adjust the MAL shape to favor imaging in that particular layer. The MAL (Dynamic Optics srl, Italy) is composed of 18 actuators and can correct up to the fourth Zernike order.[9] It has a transmission of 94% in the near infrared and a response time of less than 2ms. The MAL is positioned 2-3 cm in front of the subject's cornea, *i.e.* without strict pupil conjugation. It has a 10mm diameter, meaning that it is large enough to avoid vignetting and resolution loss which would occur with a smaller numerical aperture. Its diameter and position favor anisoplanatic correction through wavefront sensorless optimization similar to a pupil-conjugated scheme.[15,16]

To perform the optimization, we used the DONE algorithm[17] which had three major advantages for the problem we wished to solve. First, it does not require evaluation of the merit function gradient, hence mitigates the MAL hysteresis by limiting the number of times that voltages are updated. Second, the DONE algorithm is very stable due to the use of regularization and is therefore well suited for noisy experimental data. Finally, as we use the actuator voltages as input degree of freedom, no calibration step is necessary since no modal decomposition is used. The DONE algorithm models the unknown merit function using a Random Fourier Expansion (RFE) $g(x) = \sum_{k=1}^{D} c_k cos(\omega_k^T x + b_k)$ fit to the experimental data using a least square approach. It iteratively finds a minimum of the merit function on a compact set $X \subseteq [V_{min}, V_{max}]^d$ representing each actuator voltage (where $d = 18$ is the number of actuators) by updating the RFE at each new measurement, and using this RFE as a surrogate of the merit function for optimization. The number of iterations was set to 50, for a total of 1s optimization duration. Further details on the hyperparameters and the optimization steps can be found elsewhere.[18]

2.3 Imaging Acquisition and Processing

Retinal imaging was performed on three healthy near-emmetropic subjects (age range 25-31). Research procedures followed the tenets of the Declaration of Helsinki. Informed consent was obtained from subjects after the nature and possible outcomes of the study were explained. The study was authorized by the appropriate ethics review boards (CPP and ANSM - IDRCB number: 2019-A00942-55). Each subject was seated in front of the system and stabilized with a chin and forehead rest and asked to fixate a target. To maximize pupil diameter, image acquisition was performed in a dark room. Images were acquired just after wavefront optimization in parallel with real-time correction of axial eye motion. As the DONE algorithm has a high robustness to noise, subjects could blink during the wavefront optimization routine. Image sequences were composed of 150 frames acquired at 300 Hz. During image acquisition, the total power entering the eye from the FFOCT illumination source and the SD-OCT scanning source were respectively 1.3 mW (for the 0.5 s of image acquisition) and 0.25 mW (continuous scanning), which are below the ocular safety limits established by the ISO standards for group 1 devices. Since the phase of FFOCT was randomly modulated by the residual tracking error of axial motion, and to eliminate the incoherent terms, we adopted a 2-phase demodulation,[14] consisting of subtracting one image from the next and taking the absolute value. Next, images with a very low or absent signal, mainly due to an insufficient phase shift between consecutive images were automatically detected, and then excluded before registration and averaging. We used the ImageJ plugin MosaicJ[19] to stitch together five images into a $12^o \times 12^o$ FOV. A photoreceptor density map was computed using a fully automated algorithm based on modal spacing as described in.[20] Retinal fundus images of all subjects were also acquired with Spectralis scanning-laser ophtalmoscope (SLO - Heidelberg Engineering, Germany).

3. RESULTS

3.1 Increasing SNR with the Adaptive-Glasses Approach

Figure 2 shows the capacity of the adaptive-glasses approach to correct for ocular aberrations and, thus, increase the SNR at the same time for the SD-OCT and FFOCT when imaging the retina *in-vivo*. An example of the wavefront optimization time series achieved with the DONE algorithm is presented in Fig. 2(a). Here, the brightness from the cone outer segment tips (COST) was used as a merit function. An overall increase of the SD-OCT brightness can be noticed, with a maximum increase happening at the COST layer (black arrow in Fig. 2(b)), outlining that the focal plane position was optimized for this given layer.

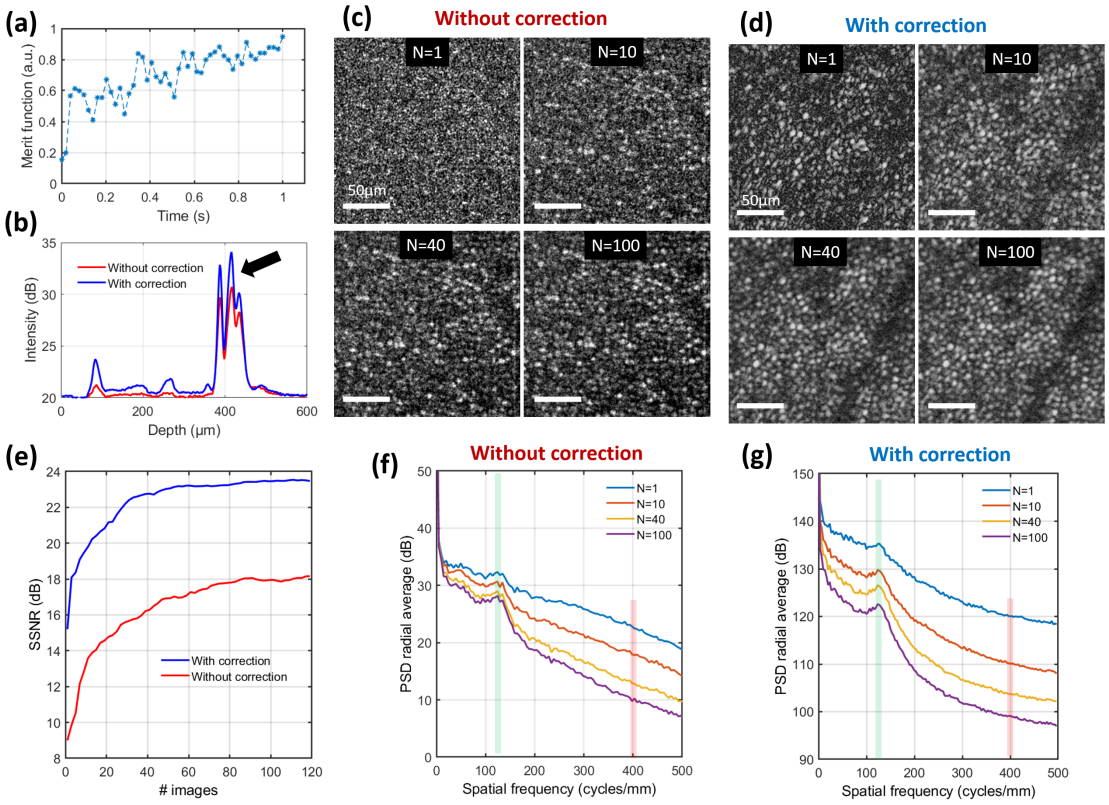

Figure 2. **(a)** Values of the merit function during wavefront optimization, for a total of 1 second duration. **(b)** Lateral average of an SD-OCT B-scan highlighting the increased signal after aberration correction. Black arrow points to the retinal layer used for wavefront optimization, *i.e.* COST. **(c,d)** FFOCT images of COST layer for different amounts of averaging (N = 1, 10, 40, 100) without **(c)** and with **(d)** aberrations correction using the adaptive-glasses approach. **(e)** Spectral SNR (SSNR) as a function of the number of averaged images with and without correcting for ocular aberrations. **(f,g)** PSD of images shown in **(c)** and **(d)** outlining the gain of SNR and how aberrations affect retinal images acquired with FFOCT. Green and red pale column are the spatial frequencies used to compute the SSNR, the former being the photoreceptor mosaic spatial frequency. Note that dB values were computed from amplitude (not intensity) signal of the FFOCT. Scale bar: $50\mu m$

Figure 2(c,d) present retinal images acquired with FFOCT from the same subject, at 4^o temporal, before and after correcting ocular aberrations with the adaptive glasses approach. Different amounts of averaging (N = 1, 10, 40, 100 images) are presented. Owing to the wavefront correction, a considerable increase of SNR can be obtained. Figure 2(e) presents the Spectral signal-to-noise ration (SSNR) as a function of the amount of averaged images with and without wavefront correction. An overall increase of 6dB of SSNR was obtained. An equivalent SSNR is obtained for N=40 without correction and N=1 with correction. The SSNR was computed using the

power spectral density (PSD) radial average data, highlighted in Fig. 2(f,g), as a ratio of the photoreceptor mosaic spatial frequency (green pale column) and noise spatial frequency (400 cycles/mm - red pale column).

The PSD data in Fig. 2(f,g) gives interesting information about FFOCT for retinal imaging. First, note that ocular aberrations do not behave as simply low-pass spatial filters as for conventional imaging systems, nevertheless aberrations affect the SNR almost equally for all spatial frequencies. Second, even without correcting for ocular aberrations, it is possible to detect the photoreceptor mosaic spatial frequency on a single non-averaged image (N=1), which is an important information to compute photoreceptor-based biomarkers such as spacing and density. Finally, using a simple strategy such as image averaging, it is possible to image photoreceptors without any aberration correction. However, this comes with a cost for the temporal resolution, making it hard to fully explore the high acquisition rate of the FFOCT, *i.e.* 300Hz, to monitor individual photoreceptors and inner-cellular dynamics. Owing to the adaptive-glasses approach, individual photoreceptors can be monitored over time with a 6ms resolution, while photoreceptor-based biomarkers can be robustly computed from the spatial frequency value.

3.2 Simultaneous High-Resolution Cross-Section and En-Face Views of the Retina in Real-Time

During each imaging session, SD-OCT B-scans are displayed in real-time. Thanks to the adaptive-glasses approach, cones formed characteristic, bold, hyper-reflective dots at the level of the inner/outer segment (IS/OS) and COST, as presented in Fig. 3(a) for a single non-averaged B-scan. Using the SD-OCT and the axial motion stabilization, one can precisely position the FFOCT coherence gate at the retinal layer of interest and explore the high axial resolution of FFOCT (*i.e.* $8\mu m$) to obtain, in real-time, en-face images from the IS/OS and COST with a $5^o \times 5^o$ FOV, as it is shown in Fig. 3(b-d). Images were acquired as close as 1^o temporal to the fovea. Photoreceptor mosaic from IS/OS and COST appeared similar, but COST signal was typically smaller than IS/OS, consistent with previous studies using AO-OCT.[21,22] Although similar, the mosaics from IS/OS and COST are not completely identical as it is shown in the false color composite image Fig. 3(e), where IS/OS coded in red, and COST in green. Signal overlap (yellow) is dominant. Green and red signal might be linked to difference of cone reflectivity, alignment, cone outer segment tip renewal and the better depiction of cone signals at the COST layer.[22]

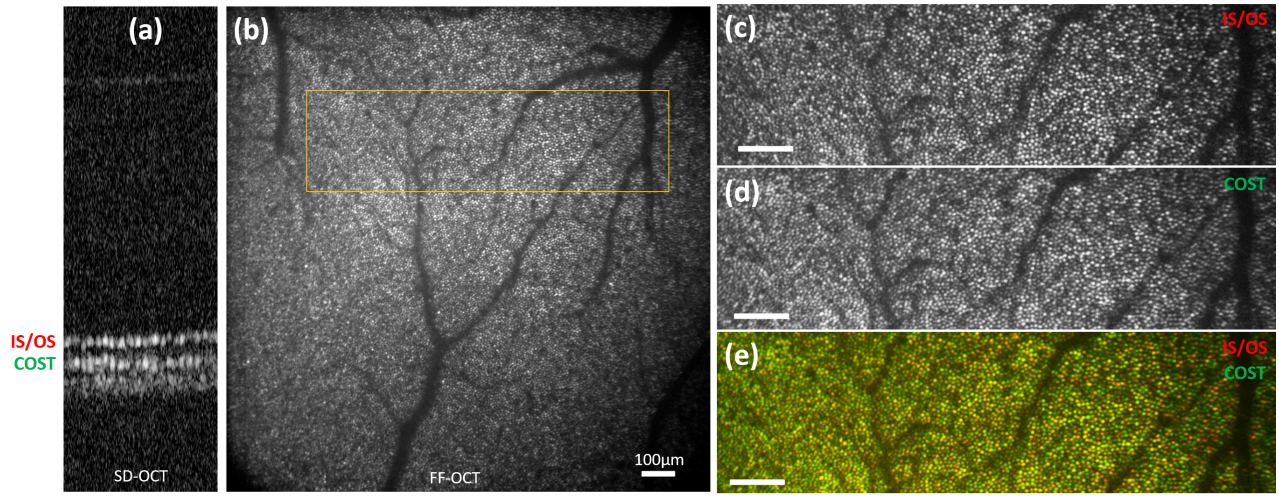

Figure 3. **(a)** Single non-averaged image of SD-OCT B-scan after correction of ocular aberrations using the adaptive-glasses approach, where individual photoreceptors from IS/OS and COST can be resolved. **(b)** $5^o \times 5^o$ FOV en-face FFOCT image acquired simultaneously to **(a)** at COST layer. Individual photoreceptors can be resolved without any apparent anisoplanetism in terms of spatial resolution. **(c,d)** FFOCT image acquired at same retinal location at the IS/OS and COST layers respectively. **(d)** is a magnified image from **(b)** (yellow box). **(e)** False color composite image of images **(c)** and **(d)** outlining the similarities and differences between the IS/OS (red) and COST (green) mosaics.

3.3 Depth-Resolved Wavefront Optimization for Inner Retina Imaging

Although the FFOCT coherence gate can be precisely positioned at the retinal layer of interest, a mismatch of the coherence gate and focal plane positions (defocus aberration) produces low SNR FFOCT images. At the full-aperture, *e.g.* for a 7-mm pupil diameter, the depth of focus is approximately ten times thinner than the retina, making focus position an essential step.[23] If the merit function does not take into account the retinal layer of interest, the wavefront optimization is biased to the photoreceptor layer,[24] preventing high SNR FFOCT images of the inner retina. To mitigate this limitation, we implemented a depth-resolved wavefront optimization, where only the brightness of the layer of interest is considered, optimizing the focal plane position to the coherence gate position. Owing to this procedure, we were able to image photoreceptor IS/OS (Fig. 4(a)) and nerve fiber layer (NFL - Fig. 4(b)) and at the same retinal region with ease, here at 8^o nasal. Green arrows, in SD-OCT B-scans, indicate the retinal layer selected as a merit function for the wavefront optimization. Owing to the high axial resolution of the FFOCT, images of NFL at different depths can be obtained, as it is shown in Fig. 4(b). Yellow and red arrows show vessels being covered by the NFL as the coherence gate position moves towards the inner retina. Blue arrow points to a vessel, where it is possible to identify the vessel wall (image on the center) and the surface reflection (image on the right).

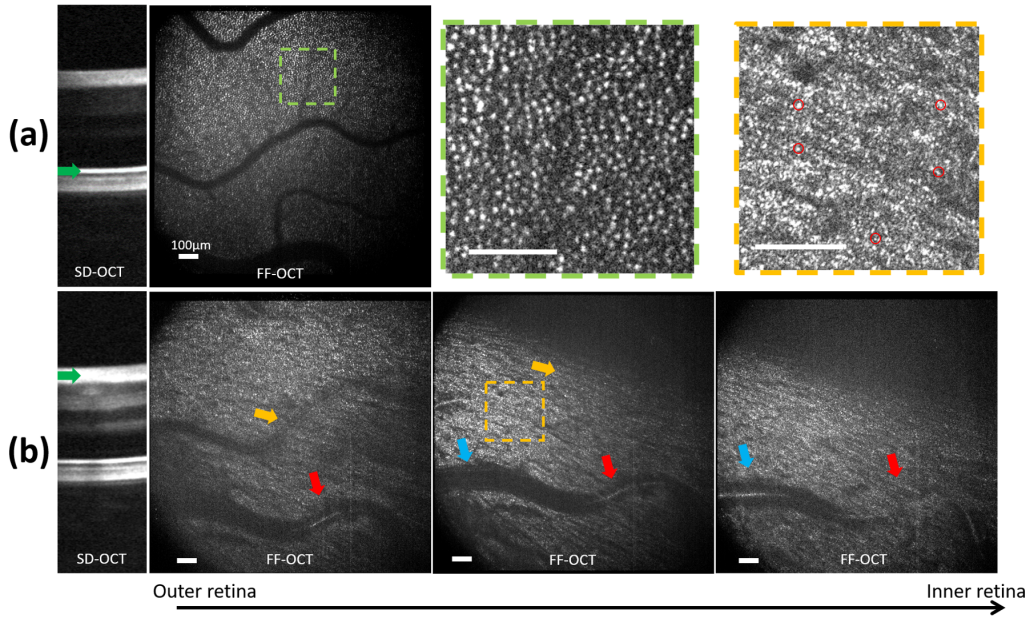

Figure 4. **(a,b)** SD-OCT retinal cross-section and FF-OCT en-face image acquired after optimizing the wavefront correction for the IS/OS and NFL layers respectively. Green and yellow dashed boxes indicate the magnified images location from the IS/OS and NFL level respectively. Individual photoreceptors and putative axonal varicosities (inside red circles) can be observed. Green arrows point to the retinal layer selected as a merit function for the wavefront optimization. Yellow and red arrows show vessels being covered by the NFL as the coherence gate position moves towards the inner retina. Blue arrow points to a vessel, where it is possible to identify the vessel wall (image on the center) and the surface reflection (image on the right). Scale bar: $100\mu m$.

One interesting retinal feature revealed by FFOCT is micron-sized hyper-reflective spots along the axon bundles (see yellow dashed box for a magnified image). These spots were already previously visible with confocal AO-SLO.[25] Their micrometer dimension is consistent with axonal varicosities.[25,26] Moreover, previous studies, using AO-SLO, had shown that the reflectivity of individual spots varies dramatically over time, potentially being indicative of axonal transport.[25] This phenomenon can also be observed in the FFOCT, but with a significantly larger FOV, higher acquisition rate and with an one order of magnitude better axial resolution. Another interesting feature observed with FFOCT is the inner limiting membrane (ILM), as it is shown in Fig. 5. As we move from NFL towards ILM, horizontal nerve fibers give place to vertical "fiber-like" structures

that might be collagen fibers that can be found in young subjects in the vitreous body close to the ILM. The PSD from the dashed white boxes also reveal the vertical "fiber-like" structure, as the vertical frequency signature from NFL becomes horizontal when close to the ILM.

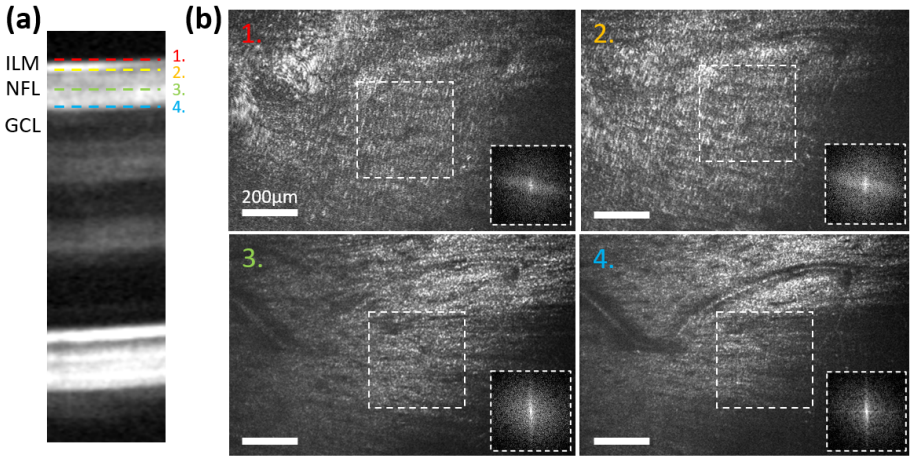

Figure 5. **(a)** SD-OCT B-scan where dashed lines indicate the depth position where the en-face FFOCT images **(b)** were acquired. White dashed boxes indicate the region of the en-face image where the PSD was computed (bottom right of each image). Scale bar: $200\mu m$.

3.4 Allying 3D High Resolution with Wide Field-of-View

One important hurdle of AO-OCT for clinical translation is the challenge of allying high-spatial resolution with a wide FOV, which is beneficial for clinical applications. Indeed, the dense sampling of the scan required comes with a cost of low acquisition rate and image distortion due to eye motion. Moreover, aberration correction using AO is limited by the eye's isoplanatic patch to a small $2^o \times 2^o$ FOV. The combination of FFOCT and the adaptive-glasses approach opens a new avenue to wide FOV high-resolution retinal imaging in a compact imaging system (system footprint: $50cm \times 30cm$). Figure 3(b) presents a $5^o \times 5^o$ FOV image obtained in a single shot (0.5s acquisition duration), as close as 1^o from the foveal center, where photoreceptors can be resolved over almost the entire FOV (limited only by the retinal curvature). Zoomed areas highlight that no apparent anisoplanatic effect in terms of spatial resolution is observed.

The wide FOV obtained in a single shot facilitates important tasks in the clinical environment to diagnose retinal disorders at early stages, such as image montaging and the computation of photoreceptor-based biomarkers.[27] Figure 6 shows two wide FOV montages from two different subjects, where the asterisk indicates the foveal center. Photoreceptor density is color coded and was consistent with the literature[28] except within 0.5^o of the fovea, where photoreceptors were not resolved but were nevertheless automatically detected using the proposed method by.[20] The montage of Fig 6(a) is composed of 5 images acquired at different retinal locations at COST layer, ranging from 11^o nasal to 7^o temporal, for a total $18^o \times 5^o$ FOV (see Fig 6(b) for a fundus image acquired with the Spectralis SLO). The montage of Fig 6(d) is composed of 6 images acquired at different retinal locations at IS/OS layer (the foveal umbo is visible), ranging from 11^o nasal to 5^o temporal, and from 5^o superior to 6^o inferior in the central portion (see Fig 6(d) for a fundus image acquired with the Spectralis SLO). Magnified images and their respective PSD are also presented. The total time necessary to obtain such images (including subject alignment, image acquisition and processing) is about 20min. For comparison, an instrument with a $2^o \times 2^o$ FOV (*i.e.*the typical size of the eye's isoplanatic patch) would need to stitch around 60 images to obtain the same image area with an image processing time multiplied by at least a factor of 10.[29,30]

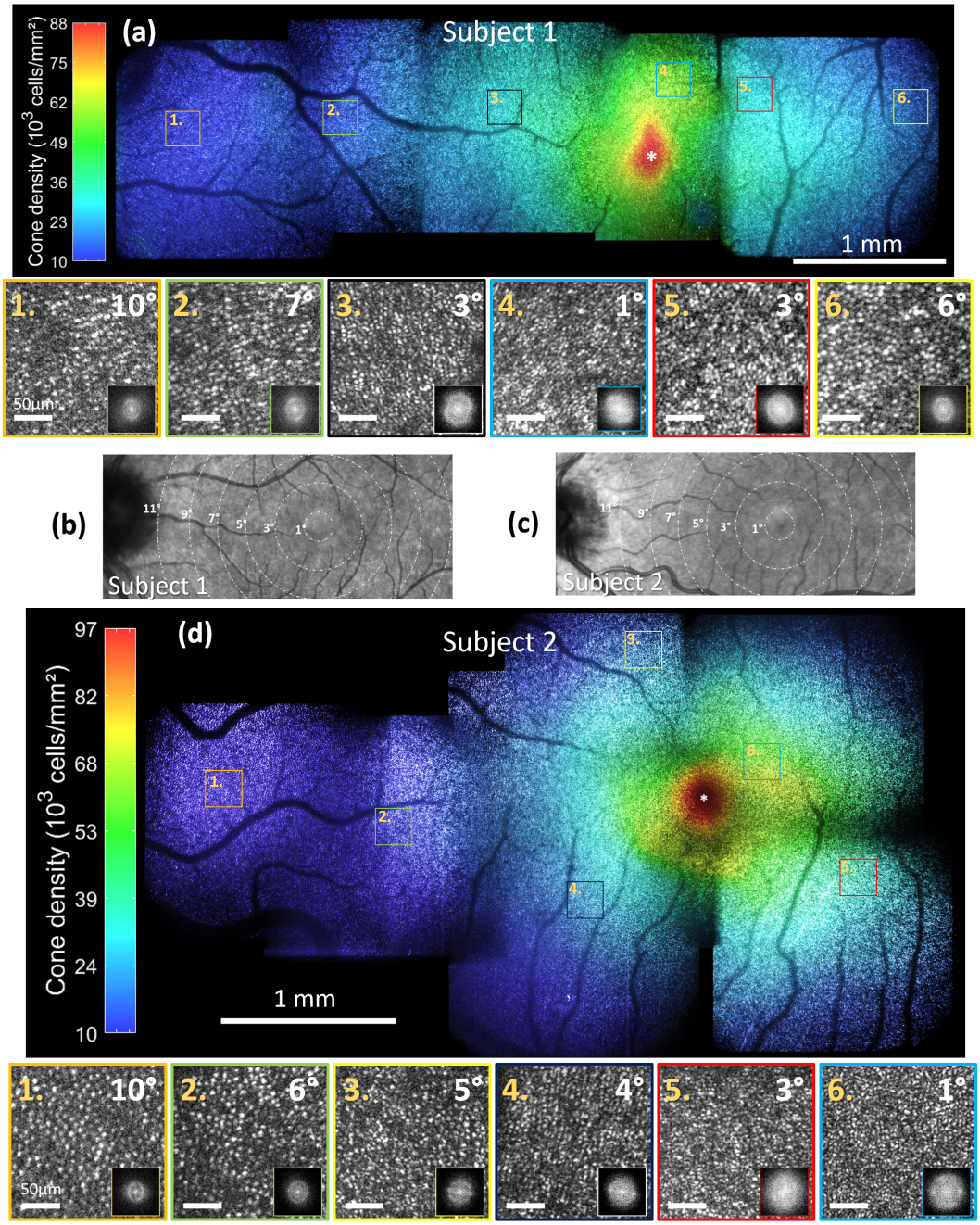

Figure 6. **(a)** FFOCT image montage from Subject 1 at COST level, with a total $18^o \times 5^o$ FOV, composed of five images stitched together. The color map and code represent the computed photoreceptor density.**(b,c)** Fundus image acquired with Spectralis SLO from Subjects 1 and 2 respectively outlining the retinal location where the FFOCT image montages were acquired. **(d)** FFOCT image montage from Subject 2 at the IS/OS level composed of six images stitched together ranging from 11^o nasal to 5^o temporal, and from 5^o superior to 6^o inferior in the central portion. Magnified images of $0.7^o \times 0.7^o$, chosen to be representative of different eccentricities, and their respective Fourier transforms are also shown. Scale bar for montages: 1mm. Scale bar for magnified images: $50\mu m$.

4. CONCLUSION

We proposed the adaptive glasses approach as a wavefront sensorless AO method favoring small footprint and low optical complexity. We successfully applied this approach to *in-vivo* retinal imaging using FFOCT to increase SNR that were previously affected by ocular aberrations. Owing to the combination of the adaptive-glasses approach with the FFOCT, we achieved 3D high-resolution retinal image over a $5^o \times 5^o$ FOV at 300Hz in a single shot, without major anisoplanatism influence. To the best of our knowledge, this is the first demonstration of AO successfully coupled to time-domain FFOCT for retinal imaging. We demonstrated that the performance achieved facilitate important tasks in the clinical environment such as image montaging and the computation of photoreceptor-based biomarkers. Photoreceptors were resolved as close as 0.5^o from the foveal center. We also showed that different retinal layers can be imaged, such as COST, IS/OS, NFL, ILM. Although we mainly illustrated the proposed approach for dual-channel SD-OCT and FFOCT retinal imaging, it can be adapted to other imaging modalities and samples. Finally, the combination of the adaptive glasses approach with FFOCT tackles those challenges that have so far prevented transfer of AO-OCT technology from bench to clinics.

ACKNOWLEDGMENTS

We thank Michel Paques and José Sahel for their clinical expertise and support. We also thank Yao Cai and Mathias Fink for technical support. HELMHOLTZ grant, European Research Council (ERC) (610110), IHU FOReSIGHT [ANR-18-IAHU-0001], Region Ile-De-France fund SESAME 4D-EYE [EX047007], French state fund CARNOT VOIR ET ENTENDRE [x16-CARN 0029-01], Fondation Visio grant, CNRS pre-maturation grant.

REFERENCES

[1] Huang, D., Swanson, E. A., Lin, C. P., Schuman, J. S., Stinson, W. G., Chang, W., Hee, M. R., Flotte, T., Gregory, K., Puliafito, C. A., and Et, A., "Optical coherence tomography," *Science* **254**, 1178–1181 (Nov. 1991).

[2] Jarosz, J., Mecê, P., Conan, J.-M., Petit, C., Paques, M., and Meimon, S., "High temporal resolution aberrometry in a 50-eye population and implications for adaptive optics error budget," *Biomed. Opt. Express* **8**, 2088–2105 (Apr 2017).

[3] Gofas-Salas, E., Mecê, P., Petit, C., Jarosz, J., Mugnier, L. M., Bonnefois, A. M., Grieve, K., Sahel, J., Paques, M., and Meimon, S., "High loop rate adaptive optics flood illumination ophthalmoscope with structured illumination capability," *Applied optics* **57**(20), 5635–5642 (2018).

[4] Jonnal, R. S., Kocaoglu, O. P., Zawadzki, R. J., Liu, Z., Miller, D. T., and Werner, J. S., "A review of adaptive optics optical coherence tomography: technical advances, scientific applications, and the future," *Investigative ophthalmology & visual science* **57**(9), OCT51–OCT68 (2016).

[5] Azimipour, M., Migacz, J. V., Zawadzki, R. J., Werner, J. S., and Jonnal, R. S., "Functional retinal imaging using adaptive optics swept-source oct at 1.6 mhz," *Optica* **6**(3), 300–303 (2019).

[6] Lassoued, A., Zhang, F., Kurokawa, K., Liu, Y., Crowell, J. A., and Miller, D. T., "Measuring dysfunction of cone photoreceptors in retinitis pigmentosa with phase-sensitive ao-oct," in [*Ophthalmic Technologies XXX*], **11218**, 1121815, International Society for Optics and Photonics (2020).

[7] Bedggood, P., Daaboul, M., Ashman, R., Smith, G., and Metha, A., "Characteristics of the human isoplanatic patch and implications for adaptive optics retinal imaging," *Journal of Biomedical Optics* **13**(2), 024008 (2008).

[8] Mecê, P., Jarosz, J., Conan, J.-M., Petit, C., Grieve, K., Paques, M., and Meimon, S., "Fixational eye movement: a negligible source of dynamic aberration," *Biomedical optics express* **9**(2), 717–727 (2018).

[9] Verstraete, H. R. G. W., Heisler, M., Ju, M. J., Wahl, D., Bliek, L., Kalkman, J., Bonora, S., Jian, Y., Verhaegen, M., and Sarunic, M. V., "Wavefront sensorless adaptive optics oct with the done algorithm for in vivo human retinal imaging," *Biomed. Opt. Express* **8**, 2261–2275 (Apr 2017).

[10] Jian, Y., Lee, S., Ju, M. J., Heisler, M., Ding, W., Zawadzki, R. J., Bonora, S., and Sarunic, M. V., "Lens-based wavefront sensorless adaptive optics swept source oct," *Scientific reports* **6**, 27620 (2016).

[11] Brunner, E., Shirazi, M. F., Laslandes, M., Drexler, W., Pollreisz, A., Hitzenberger, C. K., and Pircher, M., "Single-volume ao-oct imaging of retinal pigment epithelial cells at an extended field of view," *Investigative Ophthalmology & Visual Science* **61**(7), 224–224 (2020).

[12] Barolle, V., Scholler, J., Mecê, P., Chassot, J.-M., Groux, K., Fink, M., Boccara, A. C., and Aubry, A., "Manifestation of aberrations in full-field optical coherence tomography," *arXiv preprint arXiv:2101.09996* (2021).

[13] Mecê, P., Groux, K., Scholler, J., Thouvenin, O., Fink, M., Grieve, K., and Boccara, C., "Coherence gate shaping for wide field high-resolution in vivo retinal imaging with full-field oct," *Biomedical Optics Express* **11**(9), 4928–4941 (2020).

[14] Mecê, P., Scholler, J., Groux, K., and Boccara, C., "High-resolution in-vivo human retinal imaging using full-field oct with optical stabilization of axial motion," *Biomed. Opt. Express* **11**, 492–504 (Jan 2020).

[15] Mertz, J., Paudel, H., and Bifano, T. G., "Field of view advantage of conjugate adaptive optics in microscopy applications," *Applied Optics* **54**, 3498 (Apr. 2015).

[16] Pozzi, P., Quintavalla, M., Wong, A., Borst, J., Bonora, S., and Verhaegen, M., "Plug-and-play adaptive optics for commercial laser scanning fluorescence microscopes based on an adaptive lens," *Optics Letters* **45**(13), 3585–3588 (2020).

[17] Bliek, L., Verstraete, H. R. G. W., Verhaegen, M., and Wahls, S., "Online Optimization With Costly and Noisy Measurements Using Random Fourier Expansions," *IEEE Transactions on Neural Networks and Learning Systems* **29**, 167–182 (Jan. 2018).

[18] Scholler, J., Groux, K., Grieve, K., Boccara, C., and Mecê, P., "Adaptive-glasses time-domain ffoct for wide-field high-resolution retinal imaging with increased snr," *Optics Letters* **45**(21), 5901–5904 (2020).

[19] Thévenaz, P. and Unser, M., "User-friendly semiautomated assembly of accurate image mosaics in microscopy," *Microscopy research and technique* **70**(2), 135–146 (2007).

[20] Cooper, R. F., Aguirre, G. K., and Morgan, J. I., "Fully automated estimation of spacing and density for retinal mosaics," *Translational vision science & technology* **8**(5), 26–26 (2019).

[21] Reumueller, A., Wassermann, L., Salas, M., Schranz, M., Hacker, V., Mylonas, G., Sacu, S., Drexler, W., Pircher, M., Schmidt-Erfurth, U., et al., "Three-dimensional composition of the photoreceptor cone layers in healthy eyes using adaptive-optics optical coherence tomography (ao-oct)," *Plos one* **16**(1), e0245293 (2021).

[22] Reumueller, A., Wassermann, L., Salas, M., Schranz, M., Told, R., Kostolna, K., Drexler, W., Pircher, M., Schmidt-Erfurth, U., and Pollreisz, A., "Three-dimensional assessment of para-and perifoveal photoreceptor densities and the impact of meridians and age in healthy eyes with adaptive-optics optical coherence tomography (ao-oct)," *Optics Express* **28**(24), 36723–36739 (2020).

[23] Mecê, P., Gofas-Salas, E., Paques, M., Grieve, K., and Meimon, S., "Optical incoherence tomography: a method to generate tomographic retinal cross-sections with non-interferometric adaptive optics ophthalmoscopes," *Biomedical optics express* **11**(8), 4069–4084 (2020).

[24] Camino, A., Ng, R., Huang, J., Guo, Y., Ni, S., Jia, Y., Huang, D., and Jian, Y., "Depth-resolved optimization of a real-time sensorless adaptive optics optical coherence tomography," *Optics Letters* **45**(9), 2612–2615 (2020).

[25] Beykin, G., Norcia, A. M., Srinivasan, V. J., Dubra, A., and Goldberg, J. L., "Discovery and clinical translation of novel glaucoma biomarkers," *Progress in Retinal and Eye Research* , 100875 (2020).

[26] Wang, L., Dong, J., Cull, G., Fortune, B., and Cioffi, G. A., "Varicosities of intraretinal ganglion cell axons in human and nonhuman primates," *Investigative ophthalmology & visual science* **44**(1), 2–9 (2003).

[27] Litts, K. M., Cooper, R. F., Duncan, J. L., and Carroll, J., "Photoreceptor-based biomarkers in aoslo retinal imaging," *Investigative ophthalmology & visual science* **58**(6), BIO255–BIO267 (2017).

[28] Curcio, C. A., Sloan, K. R., Kalina, R. E., and Hendrickson, A. E., "Human photoreceptor topography," *Journal of comparative neurology* **292**(4), 497–523 (1990).

[29] Laslandes, M., Salas, M., Hitzenberger, C. K., and Pircher, M., "Increasing the field of view of adaptive optics scanning laser ophthalmoscopy," *Biomed. Opt. Express* **8**, 4811–4826 (Nov 2017).

[30] Chui, T. Y. P., Song, H., and Burns, S. A., "Adaptive-optics imaging of human cone photoreceptor distribution," *Journal of the Optical Society of America. A, Optics, image science, and vision* **25**(12), 3021 (2008).